Flexible piezoelectric AlN transducers buckled through package-induced preloading for mechanical energy harvesting

Mariello, M.; Blad, T. W.A.; Mastronardi, V. M.; Madaro, F.; Guido, F.; Staufer, U.; Tolou, N.; De Vittorio, M.

DOI
10.1016/j.nanoen.2021.105986

Publication date
2021

Document Version
Final published version

Published in
Nano Energy

Citation (APA)
Mariello, M., Blad, T. W. A., Mastronardi, V. M., Madaro, F., Guido, F., Staufer, U., Tolou, N., & De Vittorio, M. (2021). Flexible piezoelectric AlN transducers buckled through package-induced preloading for mechanical energy harvesting. *Nano Energy*, *85*, Article 105986. https://doi.org/10.1016/j.nanoen.2021.105986

Nano Energy 85 (2021) 105986

Contents lists available at ScienceDirect

Nano Energy

journal homepage: http://www.elsevier.com/locate/nanoen

Flexible piezoelectric AlN transducers buckled through package-induced preloading for mechanical energy harvesting

M. Mariello [a,b,*,1], T.W.A. Blad [c,**,1], V.M. Mastronardi [a], F. Madaro [a], F. Guido [a], U. Staufer [c], N. Tolou [c,2], M. De Vittorio [a,b,2]

[a] Center for Biomolecular Nanotechnologies, Istituto Italiano di Tecnologia, 73010 Arnesano, Lecce, Italy
[b] Department of Engineering of Innovation, Università del Salento, 73010 Arnesano, Lecce, Italy
[c] Department of Precision and Microsystems Engineering, Delft University of Technology, 2628 CD Delft, The Netherlands

ARTICLE INFO

Keywords:
Mechanical energy harvesting
Piezoelectric transducers
Aluminum Nitride (AlN)
Package-induced preloading
Compliant micro-mechanisms
Buckling

ABSTRACT

There is a high demand for novel flexible micro-devices for energy harvesting from low-frequency and random mechanical sources. The research of new functional designs is required to strategically enhance the performances and to increase the control on mechanical flexibility. In this work we report the fabrication and characterization of bi-stable and statically balanced thin-film piezoelectric transducers based on Aluminum Nitride (AlN). The device consists of a piezoelectric layer sandwiched between two thin Molybdenum electrodes that were deposited on a Kapton substrate by reactive sputtering and patterned by UV lithography. In order to improve the out-of-plane flexibility, the mechanical design is distinguished by a post-buckled flexure that introduces a negative stiffness to compensate the otherwise positive stiffness of the system. The buckling was introduced by a new method, called Package-Induced Preloading (PIP) where the mechanisms are laminated over a package with a geometry extending out-of-plane. The induced buckling resulted in bi-stable and statically balanced mechanisms which demonstrated an enhanced voltage output during a triggered snapping step. A preliminary study shows potential for the statically balanced designs and the PIP method for wind energy harvesting, revealing prospective applications and future improvements for the development of energy harvesters.

1. Introduction

Mechanical energy harvesting is a promising field that, in the last decades, has led to the development of novel micro-devices for scavenging energy from unexploited sources, such as ambient vibrations, tiny motions of the human body or low-speed fluid flows. Among the most commonly adopted transduction mechanisms for energy harvesting, the piezoelectric effect has attracted a huge interest, especially if combined with properties such as mechanical flexibility, adaptability and biocompatibility [1–10]. Piezoelectric materials directly convert applied strain energy into electrical energy and exhibit high output power densities [1,11], both, in the form of nanostructured materials [4–6] or as thin films [7–10]. Among well-known piezoelectric thin films (Lead-Zirconium-Titanate, $Pb(Zr_xTi_{1-x})O_3$, [PZT], Zink-Oxide [ZnO], Poly(vinylidene fluoride) [PVDF], Lithium Niobite [$LiNbO_3$]), Aluminium Nitride [AlN] is a suitable candidate for the development of energy harvesters for low-frequency mechanical sources due to its CMOS-fabrication compatibility, the good piezoelectric properties [12–15], and the ability to be deposited as very thin film (~1 μm) onto soft/flexible [16–21] substrates by relatively low-temperature processes such as reactive sputtering [22]. Moreover, as discussed in previous works [13,23,24], the material has a low dielectric constant (~9–11), high electromechanical coupling coefficient (~0.21), high temperature-/humidity-resistance [24], and biocompatibility [2,24], and does not need poling [16].

According to the most common theoretical models for energy

* Correspondence to: Via Eugenio Barsanti, 14, 73010 Arnesano, Lecce, Italy.
** Corresponding author.
E-mail addresses: massimo.mariello@iit.it (M. Mariello), t.w.a.blad@tudelft.nl (T.W.A. Blad), vincenzo.mastronardi@iit.it (V.M. Mastronardi), francesco.madaro@iit.it (F. Madaro), francesco.guido@iit.it (F. Guido), u.staufer@tudelft.nl (U. Staufer), nima.tolou@flexous.nl (N. Tolou), massimo.devittorio@iit.it (M. De Vittorio).
[1] Co-first authors
[2] Co-last authors

https://doi.org/10.1016/j.nanoen.2021.105986
Received 20 December 2020; Received in revised form 27 February 2021; Accepted 11 March 2021
Available online 15 March 2021

harvesters [25–27], the highest efficiency is attained at resonance, when the natural frequency of the generator is matched to the dominant frequency of the driving motion. However, for low-frequency high-amplitude motion, resonance may not be optimal for the highest efficiency due to the limited available space [25,28].

A number of low-frequency MEMS energy harvesters were demonstrated in literature. The design of Liu et al. [29], which featured a PZT cantilever designed in a S-shape, was able to harvest 1.12 nW at its resonant frequency of 27.4 Hz. In the work of Liu et al. [30] a spiral shaped PVDF cantilever was used to harvest 8.1 nW at the resonance frequency of 20 Hz. It was shown that next to the functional properties of the piezoelectric material, the output of piezoelectric energy harvesters greatly depends on the optimization of the system architecture [31–38]. This includes the use of mechanical design principles, such as the use of proof masses or buckling effects [39,40]. Yang et al. [41] studied the buckling effect and proposed a flexible energy harvester consisting of a PVDF film attached to a shell-shape substrate for energy harvesting from human motion. The folding-unfolding of the curved, pre-stressed substrate provides an increased output power in comparison to a simple flat structure. Dong et al. [42] presented a piezoelectric device, which integrates a buckled beam array design with a porous Poly(vinylidene fluoride-trifluoro ethylene) [PVDF-TrFE] thin film, for energy harvesting from cardiac motion. The maximum output open-circuit voltage and short-circuit current of the device are 4.5 V and 200 nA, respectively, with a peak-power of 49nW at an optimal resistor load of 50 MΩ. Tao et al. [43] fabricated a thermally induced bi-stable plate made of a carbon nanotube-reinforced composite with integrated piezoelectric patches for broadband energy harvesting. Guido et al. [16] proposed a pre-stressed structure [PSS] based on sputtered AlN thin films, as a piezoelectric skin for energy harvesting from folding/unfolding on human fingers. The pre-stress leads to a six-fold enhancement of the generation performances with a resulting peak-to-peak voltage of 0.7 V.

A recently adopted method to optimize the architecture of micro-devices exploits the use of negative stiffness to facilitate multi-stable systems or statically-balanced compliant micro-mechanisms [SBCM] [36,42,44]. A MEMS oscillator based on SBCM is demonstrated by Middlemiss et al. [45]. It features a proof mass on top of an anti-spring mechanism. With increasing displacement, the anti-spring softened and the system was able to reach a resonant frequency of 2.3 Hz in the vertical orientation. Another SBCM was developed and studied by Tolou et al. [46]. This mechanism was fabricated using deep reactive-ion etching and achieved a near zero stiffness characteristic over a small range of motion. Kuppens et al. [47] demonstrated a SBCM in which the preloading was induced by a MEMS compatible thin film process. The resulting mechanism combined the positive stiffness of a linear guidance mechanism with a post-buckled flexure to achieve static balancing. However, these methods are based on rigid substrates, thermal processes, or mechanical springs for reducing the stiffness, which are not suitable for achieving static balancing in very flexible transducers, therefore new approaches are needed.

In this work, we report on the development of a biocompatible and lightweight prototype of a flexible energy harvester for low-frequency motions, e.g. for wind energy harvesting. The aim is to combine flexible piezoelectric transducers with the design principles of SBCM, as illustrated in Fig. S1 (Supplementary Information 1), to build bi-stable and statically balanced devices that allow for very easy out-of-plane motions. The force-deflection relations were simulated using Finite Element Methods (FEM) and experimentally validated. Prototypes were fabricated with piezoelectric thin films of AlN deposited by reactive DC sputtering onto a soft substrate. The preloading of the device is based on a new approach, hereafter called package-induced preloading (PIP), which allows to induce buckling effects on flexible substrates by exploiting a monolithic support (package) 3D-printed at high-resolution. The prototypes have been characterized to assess the voltage and current generation properties.

2. Methods

2.1. Mechanical design

2.1.1. Piezoelectric transducers

The piezoelectric transducer is shown schematically in Fig. 1 and consists of a Kapton substrate and a piezoelectric material sandwiched between two electrodes. The following parameters can be identified; the thickness of the Kapton substrate, t_s (25 μm), the thickness of the AlN piezoelectric material, t_{AlN} (~1 μm), and the thickness of the Molybdenum (Mo) electrodes, t_e (~200 nm). The total thickness of the piezoelectric sandwich is therefore given by $t_p = t_{AlN} + 2t_e$.

The choice of Mo as electrode material is due to its properties and suitability for the AlN deposition.

2.1.2. Bi-stable and statically-balanced mechanisms

Fig. 2A shows the schematic view of the mechanism designs of the piezoelectric energy harvesters and their components. The initially flat mechanisms can be buckled by applying an axial load: this process is called preloading and results in the mechanisms assuming an out-of-plane post-buckled shape. In this post-buckled configuration, design A is a bi-stable mechanism which has a negative stiffness between the stable equilibria. In this design, a significant force must be exerted on the mechanism in order to move it through the unstable equilibrium. In order to achieve a more flexible system, static balancing can be used as a passive method to reduce the stiffness [44]. To achieve static balancing, the common approach is to add a balancer element to the mechanism in order to counteract the forces of the functional mechanism. Such a balancer should have a stiffness opposite to the stiffness of the functional mechanism [47]. In this case, the balancer element can be obtained by selectively removing material, resulting in design B. In particular, material is removed from design A over a part of the length of the mechanism such that only a narrow section (i.e. a flexure) remains. Moreover, the piezoelectric sandwich is also removed from the flexure. As a result, the post-buckled mechanism is much more compliant and it is identified as statically balanced compared to design A. Essentially, design B consists of two sections of different widths in series. During the preloading, the buckling is concentrated in the flexure due to its lower critical load. This provides a negative stiffness which compensates the positive stiffness of the wide section. The force-displacement relations of designs A and B are sketched in Fig. 2A (bottom). Besides enhancing the flexibility of the system by lowering the buckling load and reducing the stiffness (slope in the curve), the buckled shape of design B is asymmetric such that voltage cancellation as a result of opposing stresses in the piezoelectric layer is prevented, as occurs instead in design A (Fig. 2B).

The following parameters were used in the designs. In both designs the unloaded devices share the same length, L, and width, W. Additionally, in design B the flexure length, L_f, and flexure width, W_f can be identified.

2.1.3. Package-induced preloading (PIP)

In order to apply the preload, the clamping-points of the ends of the mechanisms must be moved closer to each other. In this work a new method is proposed and implemented for preloading the flat mechanisms. First, a frame was designed around the mechanism to connects its ends. The mechanism and frame are monolithically fabricated together on the same substrate. Next, the frame was laminated over a structure with a geometry extending out of plane (i.e. the package). Folding the frame over the package shortens the in-plane distance between the ends of the mechanism. This distance is reduced to the cord length of the out-of-plane curve along which the frame is folded and is smaller than the initial length L of the mechanism. It is important to note that the mechanism itself is not folded, but assumes one of its equilibrium out-of-plane positions. This process can easily be integrated in a packaging process; hence this method is proposed as package induced preloading

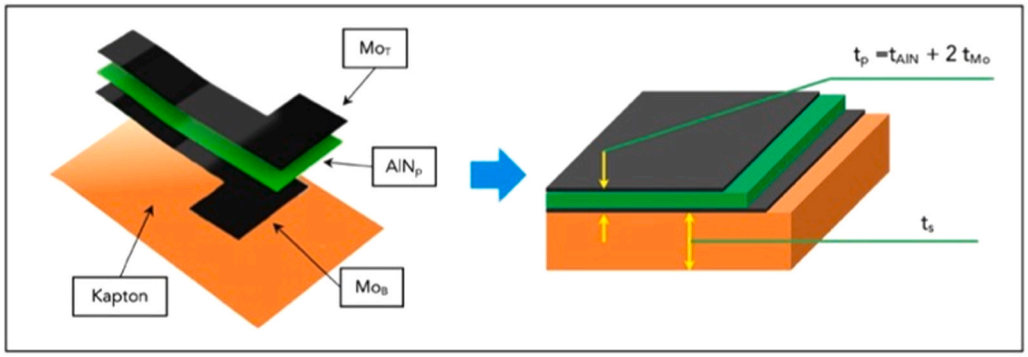

Fig. 1. Stacking sequence of deposited layers for the AlN-based flexible transducers. The right image shows the thickness parameters for the active AlN/Mo structure and for the Kapton substrate.

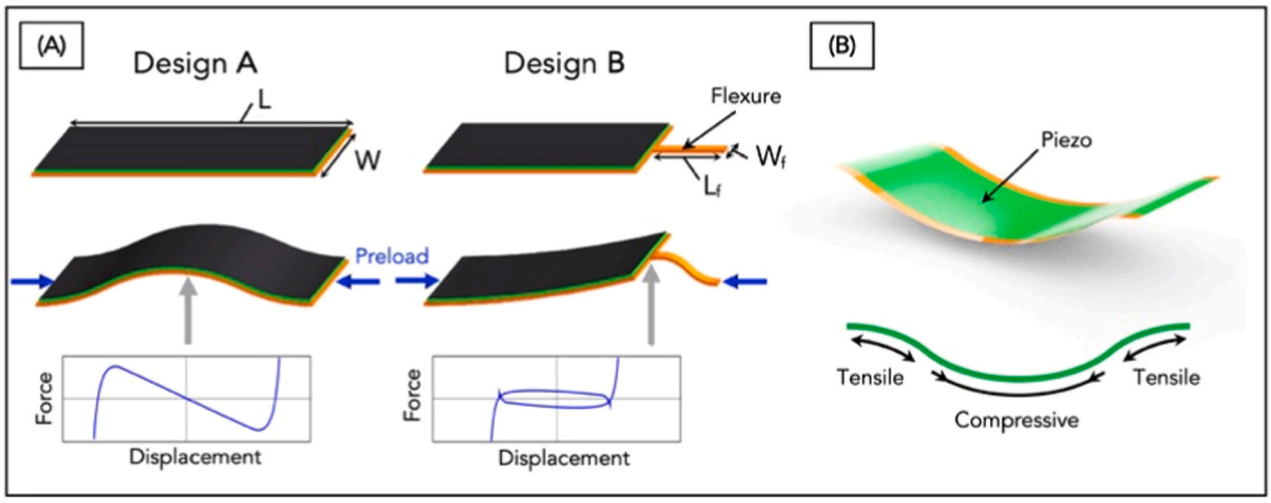

Fig. 2. (A) Comparison between the standard full configuration (design A) and the modified configuration (design B). The different mode shape for the preloaded device is depicted for the two designs as well as the corresponding force-deflection relations. (B) Charge cancellation effects due to symmetric distribution of stresses in the design A.

(PIP) and is shown in Fig. 3A(i–ii).

The proposed design for the package shown in Fig. 3B consists of ribs extending out-of-plane. The ribs are designed by tracing a path that follows three arcs with equal radii, R, in an up-down-up pattern (Fig. 3B). As a result, the absolute value of the curvature is constant over the whole curve. The preloading displacement, dL, is defined as the difference between the initial length L, of the mechanism, and the new, after-packaging straight length (or shortened length) D, and is given by the following equation, as a function of the radius and length:

$$dL = L - D = \quad L - 4R\sin\left(\frac{L}{4R}\right) \tag{1}$$

Moreover, the equilibrium positions x_{eq} of the post buckled symmetric mechanism (design A) can be easily found as approximately equal to the height H of the ribs according to the following formula (Fig. 3C):

$$x_{eq} = 4R\sin^2\left(\frac{L}{8R}\right) \quad \approx \quad \frac{L}{\sqrt{6\cdot dL/L}}\sin^2\frac{\sqrt{6\cdot dL/L}}{2} \tag{2}$$

Therefore, the predicted out-of-plane range of motion for this buckling structure is given by:

$$\Delta = 2x_{eq} \tag{3}$$

The aforementioned parameters for the mechanism of design B are more complex and require computational simulations to be calculated.

2.1.4. Design parameter variations

Fig. 4A illustrates the planar mechanism B with indication of the components, whereas Fig. 4B reports an exploded view of the final PIP device, representing the whole system comprising transducer, mechanism and package.

In Table 1 the complete list of geometrical parameters for the fabricated PIP prototypes is reported. Multiple versions of design B were fabricated in which the lengths of the flexure and the piezoelectric area were varied. The motivation for this was not to perform an optimization of these design parameter for a particular application, but rather to allow a preliminary investigation on the performances of different design variations. The nomenclature that will be used to identify the variations in the design is set as follows. *B1-B4* are variations of design B, where $L_S = L - L_f$ is the length of the wide section. *B1* and *B2* stand for the devices with a full piezoelectric area with short and long Kapton flexure, respectively. *B3* and *B4* correspond to devices where the piezoelectric area covers only part of the wide section namely for up to the length L_p. The uncovered Kapton area of width W and length $L_S - L_p$ is called collector area.

2.2. Fabrication

2.2.1. Materials

Silicon wafers were used as support for the sputter-deposition of the piezoelectric stack.

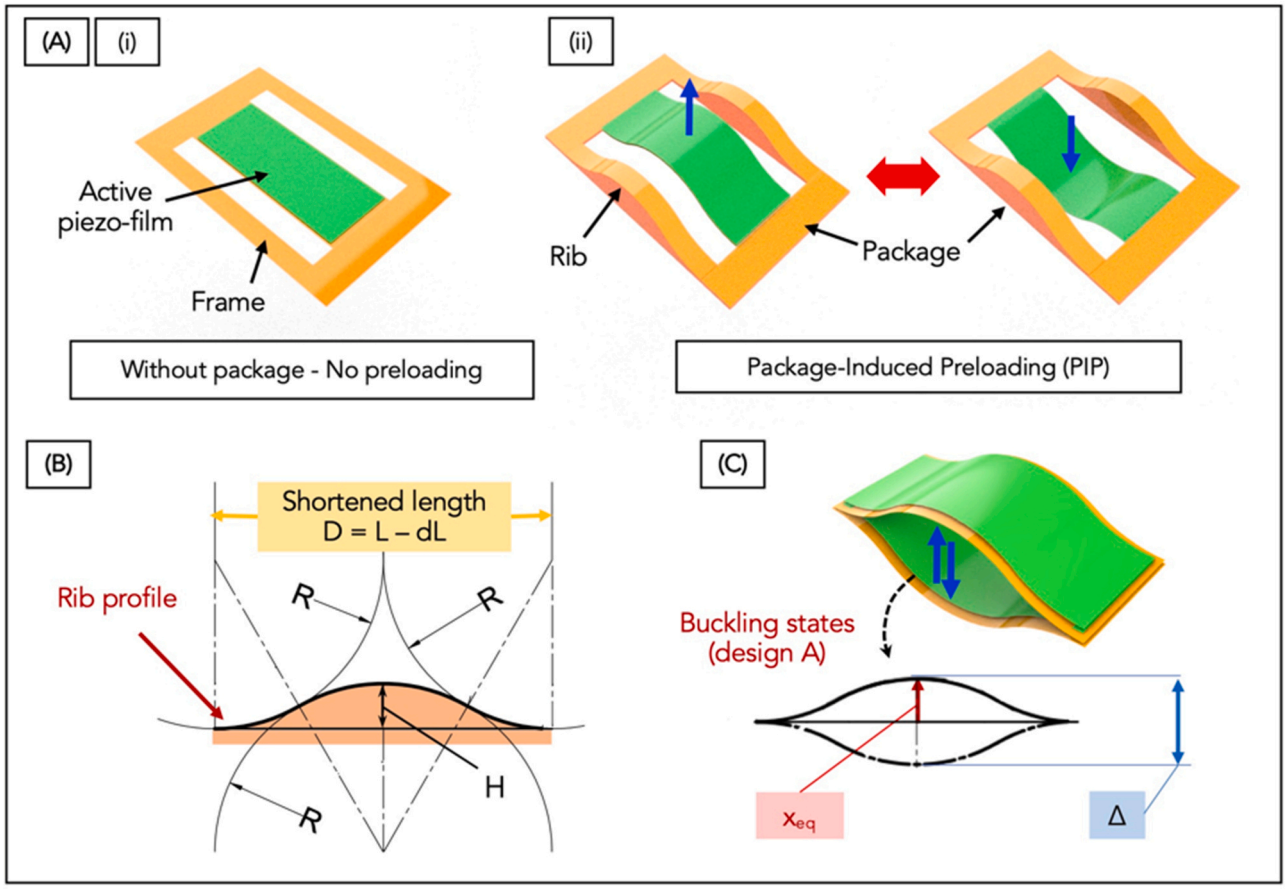

Fig. 3. (A) Conceptual scheme of Package-induced Preloading (PIP): (i) flat flexible transducers without package: no buckling or preloading occurs. (ii) Package-Induced Preloading (PIP) due to properly designed package, with out-of-plane ribs. (B) Profile of the curved frame (rib) (i) with indication of the geometrical parameters used in sizing and the theoretical amplitudes of the buckling states for design A (ii).

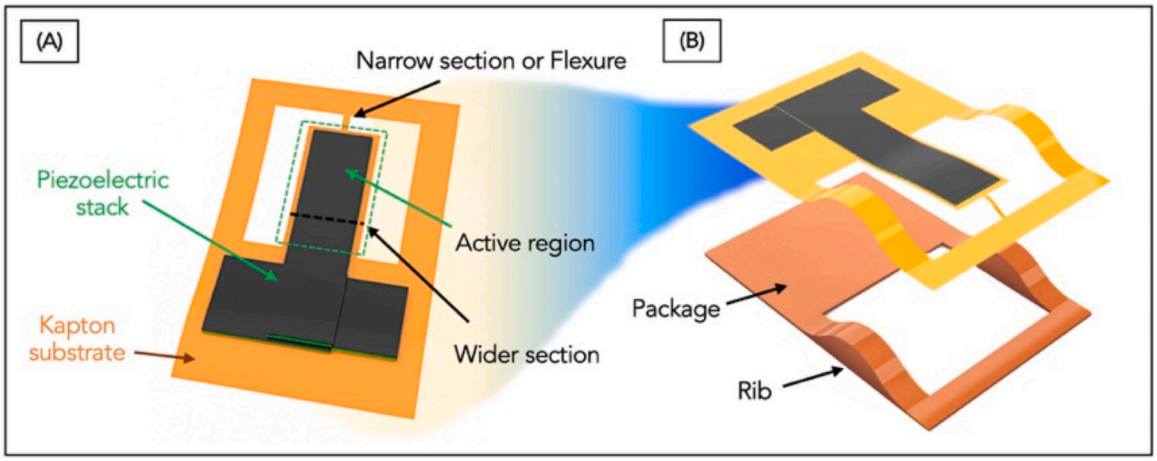

Fig. 4. (A) Design for the planar mechanism, consisting of Kapton substrate and a proper active piezoelectric area, with indication of the main parameters. (B) Exploded view of the planar mechanism on the package used in this work.

PolyDiMethyl Siloxane (PDMS) (Sylgard 184 Silicone Elastomer) was supplied by Dow Corning Corporation in two compounds: a viscous uncured pre-polymer and a curing agent. Kapton HN 25 μm-thick foils were supplied by DuPont. The rigid frame was 3D-printed utilizing a dielectric ink (Dielectric Nanoparticle Polymer Ink) for the insulating support. A double-adhesive tape (3M™ ECATT 9703) was used for assembling the device.

2.2.2. *Piezoelectric transducers*

The realization of the thin-film piezoelectric transducers followed a previously reported microfabrication process [16,17,49,50]. In brief, the Kapton substrate was attached to a silicon wafer using ~160 μm-thick PDMS spin-coated at 500 rpm for 30 s, degassed under vacuum to remove entrapped residual air-bubbles, then cured at 90 °C for 15 min. The piezoelectric stack was deposited by reactive sputtering (K.J. Lesker Lab 18 system) in two single runs in order to minimize

Table 1
Geometrical parameters of the fabricated PIP prototypes.

Parameter	Symbol	Value				
Transducers						
Substrate thickness (μm)	t_s	25				
Piezo stack thickness (μm)	t_p	1.6				
Mechanisms		**A**	**B1**	**B2**	**B3**	**B4**
Flexure length (mm)	L_f	–	1.9	7.9	4.9	1.9
Flexure width (mm)	W_f	–	0.38	0.38	0.38	0.38
Wide section length (mm)	L_s	15	13.1	7.1	10.1	13.1
Wide section width (mm)	W	7	7	7	7	7
Piezo length (mm)	L_p	15	13.1	7.1	7.1	7.1
Package						
Rib radius (mm)	R	5				
Rib height (mm)	H	2.7				
Preloading displacement (mm)	dL	1.5				
Shortened length (mm)	D	13.5				

contaminations. A 120 nm-thick AlN interlayer and the bottom Mo-electrode (200 nm) were deposited in a single step and patterned by optical UV lithography and chemical etching (Fig. 5A(i)). In a similar way, the AlN piezoelectric layer (~1 μm) and the second top Mo-electrode (200 nm) were deposited in a single run by sputtering (Fig. 5A(ii)) and subsequently patterned through dry etching with Inductively-coupled Plasma-Reactive Ion Etching (ICP-RIE) system (Fig. 5A(iii)). The detailed process parameters used for the sputtering deposition and for the etching step are reported in Supplementary Information 2. The residual stress induced in the deposited thin-film stack is due to the temperature reached during the sputtering process: up to ~70 °C and to ~165 °C for the Mo and AlN steps, respectively.

2.2.3. Assembly

A CO_2 laser micro-machining system (from Universal Laser Systems, VLS2.30) has been employed to perform the laser cutting process on Kapton (Fig. 5A(iv)). The description of the setup and technical details are reported in the Supplementary Information 3, in particular in Fig. S2 (i).

The laser process parameters were optimized to ensure a smooth cut-through performance and clear releasing of samples [51]. In particular, a laser power of 9 W, a scanning speed of 63 m/min and a pulse density of 750 ppi were adopted. A complete summary of the laser parameters is given in Table S1, and a resulting cut line is reported in Fig. S2(ii).

Afterwards, the devices were immersed in Isopropyl Alcohol and ultrasonically cleaned for 30 s, to remove any traces of carbonaceous residues resulting from the ablation of polyimide [52,53].

The package was printed by a multi-layer 3D PCB printer (DragonFly LDM™ System, Nano Dimension) and used as support for the flexible piezoelectric transducers. The 3D printing process took approximately 6 h and it consisted of inkjet printing and curing simultaneously a dielectric ink at ~70 °C.

The final devices were assembled as illustrated in Fig. 5A(v, vi) and Fig. 5B: a double-adhesive tape was shaped by laser cutting, aligned and attached onto the 3D printed frame. Subsequently, the AlN-based flat transducers were laser-cut and peeled off from the PDMS/Si substrate with the aid of an upper adhesive tape (Fig. 5A(v, vi)). Finally, the free-standing transducers were allowed to slowly adhere onto the double-adhesive tape (Fig. 5B). The electrical connections were made on the exposed pads of the bottom and top electrodes, by using an adhesive Copper (Cu) tape, rivets and electrical wires: Silver paste and soldering Tin were used to improve the conduction of the connections. Fig. 5C reports a real photo of a PIP device after the entire fabrication process.

2.3. Simulations

To simulate the mechanical behavior of the buckled structure a finite element model was built in ANSYS using beam elements (beam188). The composite cross-sections of the piezoelectric transducers were modeled as cross-sections of a custom uniform material. Eq. (4) was used to determine the elastic modulus such that the flexural rigidity of the custom-material cross section matched that of the composite cross-

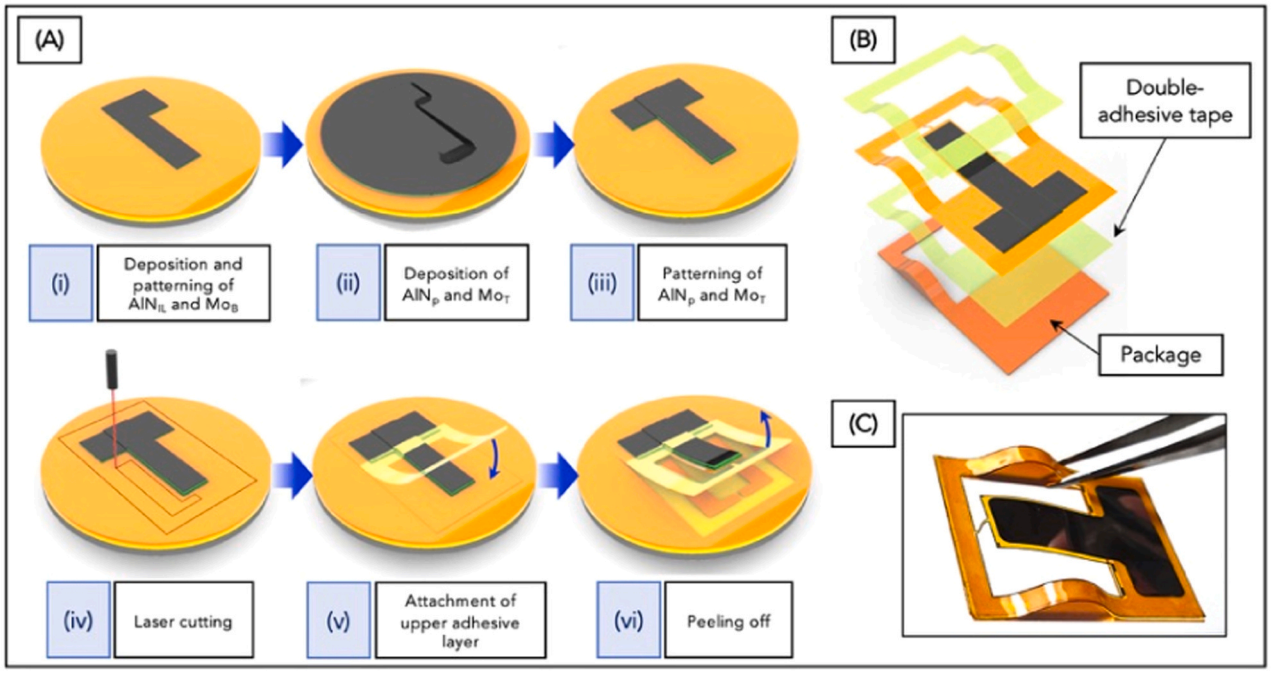

Fig. 5. (A) Detailed fabrication and assembly process of the PIP devices. (i) Deposition and patterning of AlN interlayer and Mo bottom electrode. (ii) Deposition of AlN piezoelectric layer and Mo top electrode. (iii) Patterning of AlN piezoelectric layer and Mo top electrode. (iv) Laser cutting. (v) Attachment of adhesive layer. (vi) Peeling off. (B) Attachment of the flexible structure onto the 3D printed package through double-adhesive tape (C) Real photo of a PIP device after the fabrication and assembly process.

section using the parallel axis theorem:

$$EI_{eq} = \sum_{n}^{N} \frac{E_n w {t_n}^3}{12} + E_n w t_n {y_n}^2 \quad (4)$$

where y_n is the distance with respect to the neutral axis of the middle axis of the composite cross section; E_n, t_n are the Young's modulus and the thickness of the n^{th} layer, respectively.

The materials are assumed to be perfectly elastic with the properties listed in Table 2.

Buckling was induced by constraining one end of the mechanism in all directions, and moving the other end by the same amount as expected from the PIP. Small imperfections were incorporated in the mechanism to prevent the simulation to crash due to singularities in this preloading step. After the buckled shape was achieved, a displacement was applied to the node with the maximum out-of-plane displacement to flip the mechanism to its other stable configuration. During this, the reaction forces are recorded at regular intervals to determine the force-deflection behavior.

2.4. Mechanical and electrical characterization

For measuring the out-of-plane force-deflection behavior of the fabricated devices, the measurement setup reported in Fig. 6A(i–ii) was used. A microforce sensing probe (FUTEK LRM200) with a resolution of 0.5 μN (1) is mounted on the mechanism (2) and displaced by a precision linear stage (Physik Instrumente M-505) with a resolution of 8.5 nm (3), from which the internal encoder captures position data. Data was recorded using a NI USB-6008 (4) in 250 steps over the range of motion.

The electrical properties (impedance, phase, capacitance) of the thin-film piezoelectric stack were measured by connecting the device to an Agilent E4980A Precision Inductance-Capacitance-Resistance (LCR) meter and performing frequency sweeps.

The devices were evaluated by mechanically triggering the snapping state of the fabricated devices at ~1÷2 Hz and by detecting the open-circuit voltage with an oscilloscope (Textronix MDO 4104-3). The applied load for these tests consisted of a mechanical stimulus triggered by a linear micro-actuator (by Actuonix Motion Devices Inc., L16-R, 100 mm, 35:1, 6vdc), which served to allow the fast snapping transition between the two equilibrium positions of the bi-stable element.

The 3D printed frames were characterized in terms of mechanical strength and flexibility, since they serve as support for the flexible transducers, thus they must be lightweight and resistant to some extent. Dynamic mechanical analysis (DMA) measurements were performed in controlled force mode (force rate 1 N/min) with a Q800 instrument (TA Instruments). The details for the mechanical testing conditions are reported in Supplementary Information 5.

2.5. Application testing

To demonstrate the potential of the flexible PIP devices for low-frequency energy harvesting applications, their performance was studied in a custom setup for wind energy harvesting. The setup is shown in Fig. 6B(i–iii): it is based on a standard suction subsonic wind tunnel (provided by TQ TecQuipment), with a working section of $30.5 \times 30.5\ cm^2$ and 60 cm long, enclosed by acrylic side-walls. A detailed description of the equipment is reported in Supplementary Information 6. A custom-built setup based on an Arduino-controlled stepper motor allows to set speed parameters from a suitable computer, up to 20 m/s (Fig. 6B(iii)). In particular, a wind speed ramp has been set in the range 0÷20 m/s with a step of 2.5 m/s for a time interval of 5 s. Inside the working space of the wind tunnel, the devices are fixed between two halves of a bluff body (Fig. 6B(ii)) which has been positioned at 0° with respect to the incoming wind flow. The aim of the bluff body, according to the theory of flow by T. von Karman [57], is to induce a flow separation and to generate a Karman vortex street downstream of the body itself. The forces resulting from shedding vortices and periodic pressure gradients are responsible of the periodic vibration/oscillation of the structure attached to the bluff body [58]. The bluff body has a reverse C cross section because it has been demonstrated as the best shape to optimize the generation of vortices downstream of the device [59–61]. The transversal pressure variation can be determined in terms of pressure fluctuation coefficient $C_p = \Delta p / \left(\frac{1}{2}\rho v^2\right)$, where ρ, v are the air density and the free-stream wind speed [62,63]. Specific aerodynamics experimental studies would be necessary to obtain spatial distribution spectra of C_p. The effective area interested by the pressure fluctuations is the area of the oscillating element, i.e. $L_s \cdot W$. The mechanical strain energy periodically induced in the flexible structure is then converted into electrical energy by the direct piezoelectric effect.

Therefore, the bluff body has three functions: (i) it acts as splitter for the incoming airflow, generating vortices and turbulences, (ii) serves as a fixed clamp for the device; and (iii) it contains and protects the electrical wires that are feed to the outside of the wind tunnel through the acrylic side-walls of the working section.

The devices are positioned parallel to the airflow (i.e. at 0° with respect to the flow direction), downstream of the bluff body. Additionally, in order to avoid edge effects, they are placed at middle height of the working section and at 20 cm from the inlet.

The power curves were obtained by measuring the voltage drop on different resistive loads connected to the devices. The maximum power is reached when the device is electronically terminate with an optimal load that matches its electrical impedance [64].

Table 2
Materials properties used for FEM simulations.

Material	Properties	Ref.
Kapton	$\rho = 1.42\ g/cm^3$; E = 2.5 GPa; $\nu = 0.34$;	[54]
AlN	$\rho = 3.26\ g/cm^3$; E = 330 GPa; $\nu = 0.22$;	[12,13,15,55,56]

ρ mass density; E Young's modulus; ν Poisson's ratio.

3. Results and discussion

3.1. Fabricated prototypes

The sputter-deposition of AlN onto the Kapton substrate has produced a crack-free, 1 μm-thick, transparent piezoelectric film. Fig. S3A (i–iv) show the stacking sequence of layers after the deposition and lithography processes, as well as the cross-section and morphology. The columnar arrangement of the AlN-nanograins along the c-axis(0002) direction yields a wurtzite-phase polycrystalline lattice. This result is strictly affected by the sputtering process and also by the nature of the metal substrate. The choice and effect of Mo as metal electrode is discussed in Supplementary Information 4, based on previous works [12, 65,66–68]. Supplementary Information 4 also reports the details of the characterization of the AlN thin films deposited onto the flexible substrate, in terms of crystallographic phase, through X-ray Diffraction (XRD) and Piezo-response Force Microscopy (PFM); tensile rigidity, through Dynamic Mechanical Analysis (DMA), residual internal pre-stress induced by the sputtering process, and electrical impedance/capacitance.

The surface of the Kapton structure proofed clean and undamaged after laser cutting (Fig. S2(ii)), allowing a smooth and debris-free peeling from the Si substrate. Fig. S4A(i) depicts the package after 3D printing. The detailed morphological (AFM) and mechanical (DMA) analyses of the package are described in Supplementary Information 5. It exhibits a high compliance maintaining the necessary robustness to act as mechanical support, thus it is suitable for the fabrication and assembly of lightweight and flexible energy harvesters.

The final PIP devices, after cutting and assembly, are illustrated in

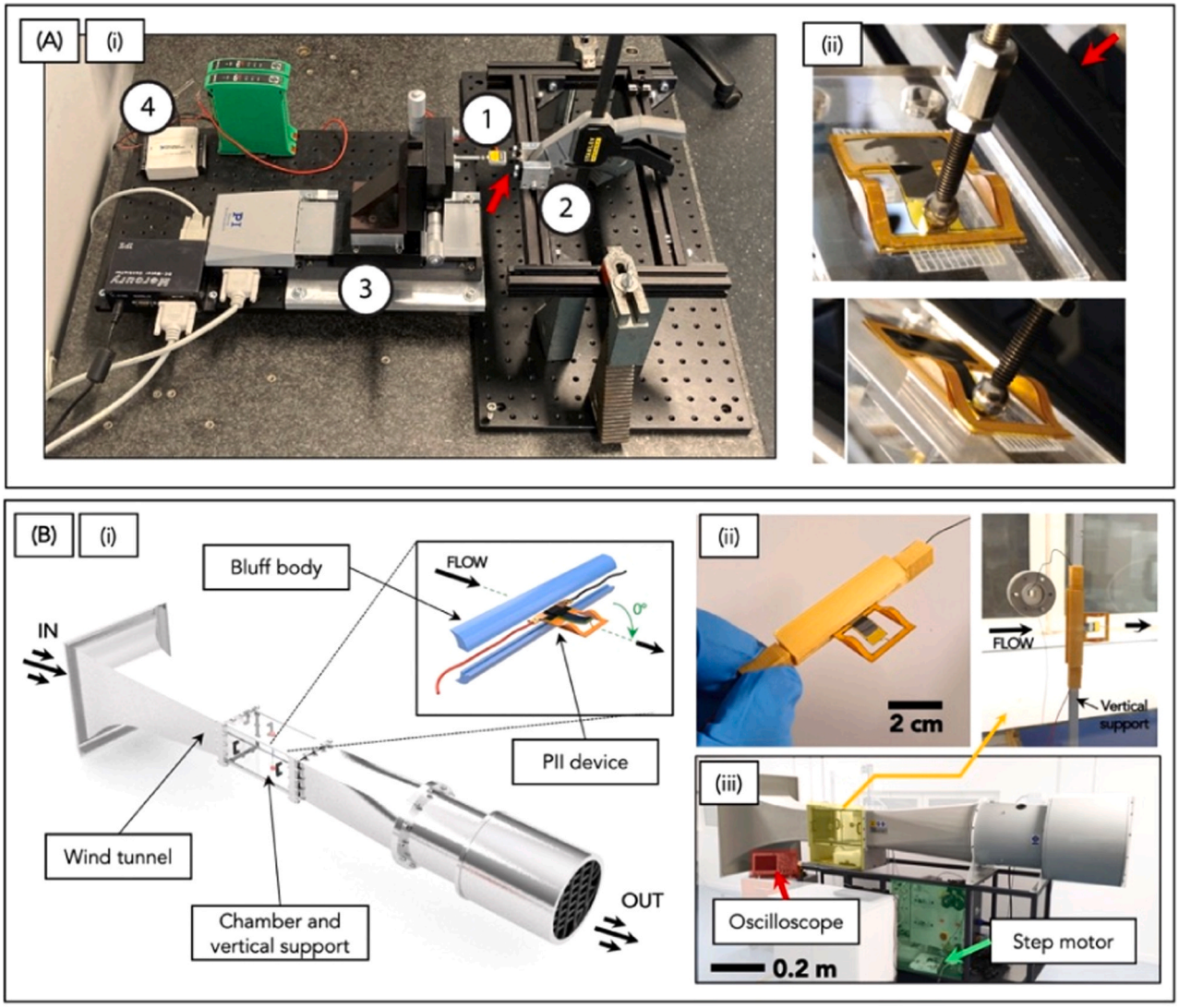

Fig. 6. (A) (i) Photo of the force-deflection measurement setup with (1) microforce sensing probe, (2) mechanism, (3) precision linear stage, (4) data recorder. (ii) Closeup of a real sample being tested. **(B)** Wind tunnel setup employed for wind energy harvesting tests (i), with the PIP device fixed inside a 3D printed bluff body (ii). The position and direction of the device with respect to the wind flow are indicated. The step motor allows the controlled variation of wind speed and the oscilloscope is used to detect the signal from the device (iii).

Fig. 7A(i, ii), whereas Fig. 7B(i–v) summarize the different designs tested in this work, in order to evaluate the influence of some geometrical parameters, i.e. the length of the piezoelectric area and the length of the narrow Kapton flexure. The pictures of the transducers after peeling and of the devices after assembly are reported together with the nomenclature used for referring to each design.

3.2. Force-deflection measurements

The force-deflection relations of the mechanisms are shown in Fig. 8 for the simulation and the experiment. From the figure it can be observed that the flexibility for devices B1-B4 is improved compared to device A, due to the lower stiffnesses (Fig. 8A(i)). Fig. 8A(ii) shows in a magnified view an overlapping comparison of the force-deflection curves for the other designs (B1-B4).

Fig. 8B demonstrates a typical theoretical force-deflection relation of a bi-stable system (black curve). Three equilibrium positions are found on the curve where force is equal to 0. Two of these positions (i.e. points 1 and 4) are stable equilibria where the system has a positive stiffness, and the other position is an unstable equilibrium (i.e. point 3) where the system has a negative stiffness. Moreover, in point 2 a maximum in the force-deflection relation can be found, which is identified as the switching point [69]. When the system is loaded past the unstable equilibrium, snap-through occurs and pulls the system to the opposite stable configuration.

The force-deflection relations of the post buckled devices A and B1-B4 are reported for each design in Fig. 8, whereas as reference a similar typical curve is illustrated in Fig. 8B (green curve). These curves show two bifurcation points between which two load paths can be identified (i.e. points 5 in Fig. 8B). This section of the curve between the bifurcation points is identified as the low-stiffness region (LSR). It can be observed that, outside the LSR, the force-deflection relation rapidly steepens. This steepening effect is a result of strain hardening, which occurs because the devices are straightened and loaded in tension. The two load paths within the LSR correspond to the two configurations of the system that can be identified as “knee-up” and “knee-down” and are present due to the rotational degree of freedom at the point where the force-deflection relation is measured. The peaks that are found in the simulated responses are the result of the snap-through behavior that occurs when the system changes between the configurations. In Fig. 8C

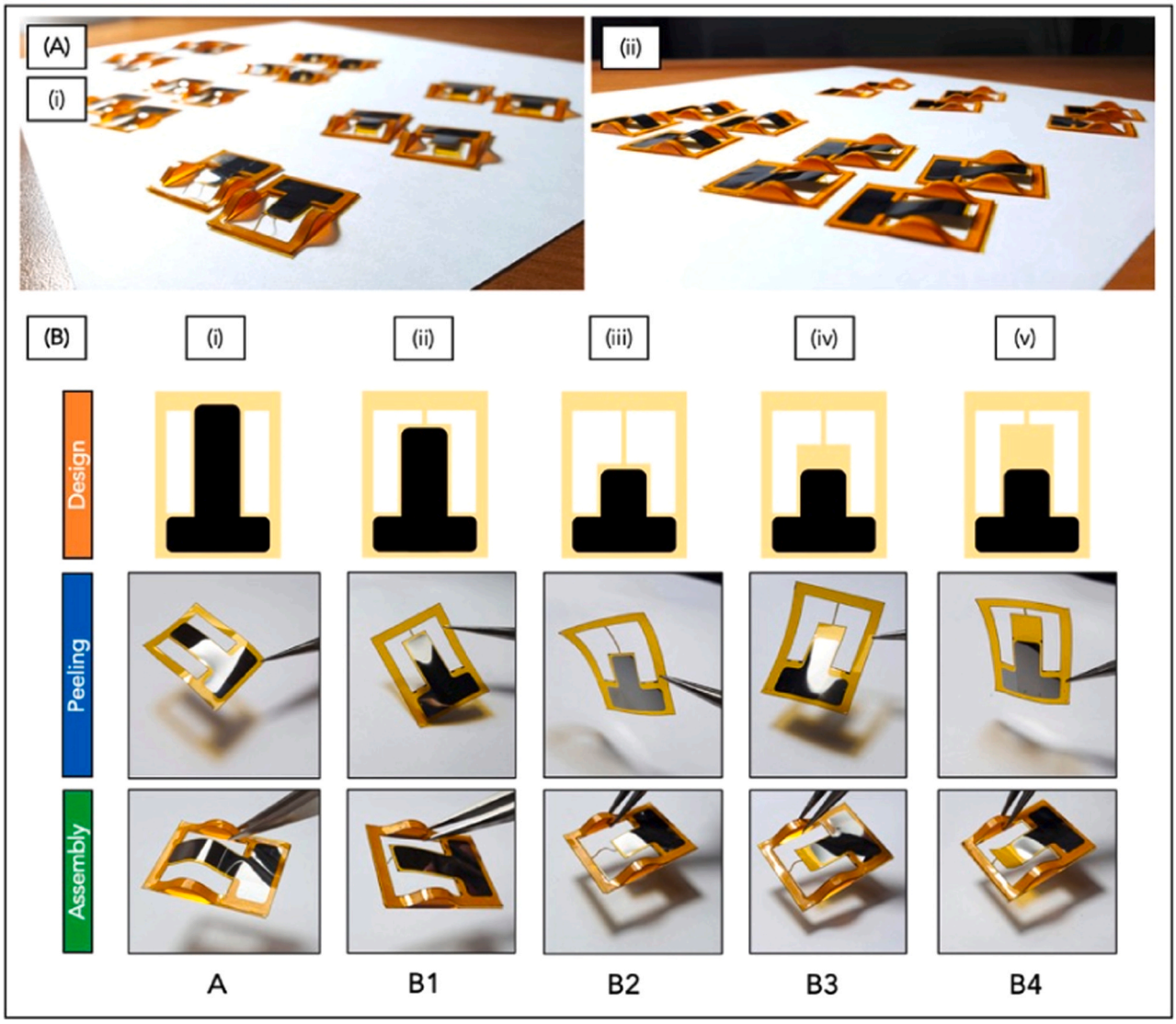

Fig. 7. (A) (i, ii) Assembled PIP devices with different designs for the piezoelectric transducers. (B) Several tested designs with different geometrical parameters: design, pictures of the transducers after peeling and picture of the assembled PIP devices. The nomenclature of the designs (A, B1-B4) is set as follows. (i) Design without narrow stripe (design A). (ii) Design with a long piezoelectric area (design B1). (iii–iv) Design with a short piezoelectric area with different lengths for the Kapton narrow stripe, i.e. long (B2), intermediate (B3) and short (B4), respectively.

the force-deflection relation of the bi-stable device A is shown, which acts as a reference for the statically balanced designs B1-B4. It can be observed that the force at the switching point of device A is 16 mN and that the device has a range of motion of almost 6 mm between the equilibrium positions. Fig. 8(D,G) show the force-deflection relations of devices B1 and B4 respectively, where the force at the switching point was reduced to 7 mN and 2 mN, respectively, as a result of the narrow flexure. However, in these devices the range of motion is reduced to approximately 3 mm and 3.5 mm. Fig. 8(E,F) demonstrate the force-deflection relations of the designs B2 and B3. A force at the switching point of 2 mN and a range of motion of 3 mm were found for Device B3. Device B2 was found to have a single equilibrium position at 0 mm and very slight positive stiffness. From Fig. 8 it can be observed that the effect of static balancing using the narrow flexure was demonstrated to result in more flexible systems, and that in most cases the simulated force-deflection relations show good correspondence to the measurements. The most apparent differences between simulation and experiments are discussed next.

In general, slightly larger forces were experimentally measured compared to the simulated results, which can be explained by deviations in material properties and dimensions as a result of fabrication. Additionally, some measurements show asymmetry in their force-deflection relations while all simulations are symmetric. This is particularly evident in the bi-stable device shown in Fig. 8C. The main reason for this is that the system is modeled as a custom uniform material, where in reality the cross-section is built from multiple layers with different properties. While this should not directly lead to an asymmetric force-deflection relation, the combination with residual stresses in some of these layers as a result of the fabrication process is very likely to cause this asymmetry. Moreover, the probe that was used during the measurements has a finite size and therefore it was not possible to actuate the devices exactly at the interface between the wide and narrow sections. Lastly, in devices B3 and B4 visual clues of residual stresses as a result of the fabrication process were observed in the wide Kapton sections between the AlN and the narrow flexure. This can explain the mismatch between the simulated and measured force-deflection curves particularly for these devices.

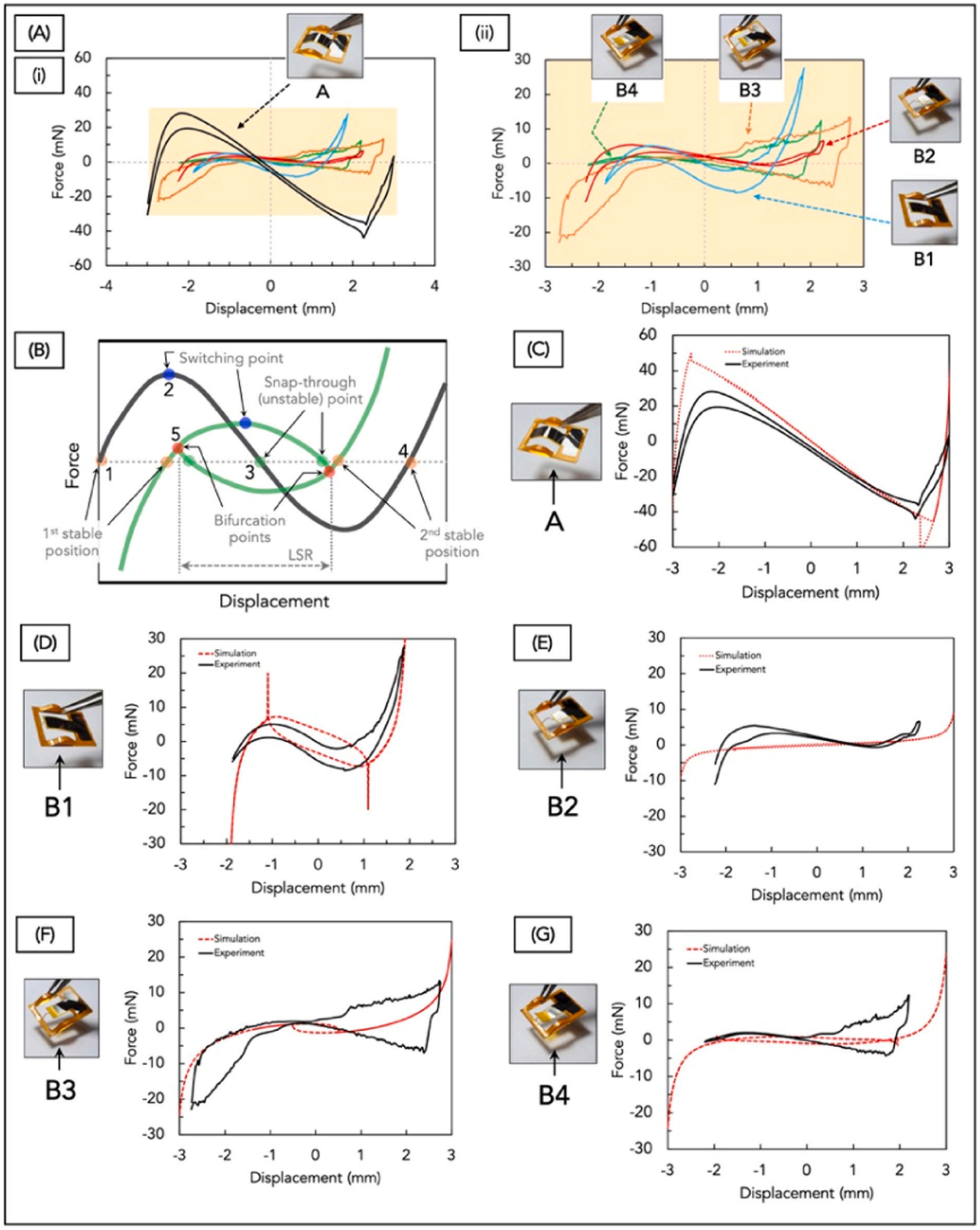

Fig. 8. (A) (i, ii) Force-deflection curves of the different selected devices: the reduction of stiffness can be clearly observed from the design A to the other designs. (B) Example of a force-deflection curve for design A (black) and a statically-balanced design B (green), with indication of the first stable position (1), the switching points (2), the snap-through points (3), the second stable position (4), the bifurcation points (5) and the low-stiffness region (LSR) of a generic snapping structure. (C–G) Force-deflection curves for each single tested design, compared with the simulated curves.

3.3. Influence of buckling onto the output generation

Preliminary performances of the fabricated PIP devices have been conducted by triggering the snapping state of the unstable structures, and detecting the output open-circuit voltage by means of an oscilloscope. Fig. 9A depicts the forward and backward snapping of a PIP device, whereas Fig. 9B reports the signals of the PIP devices with different designs. The comparison between the fixed device with only thermal stresses and the devices with package-induced instability reveals an enhancement of the generated voltage owing to the fast

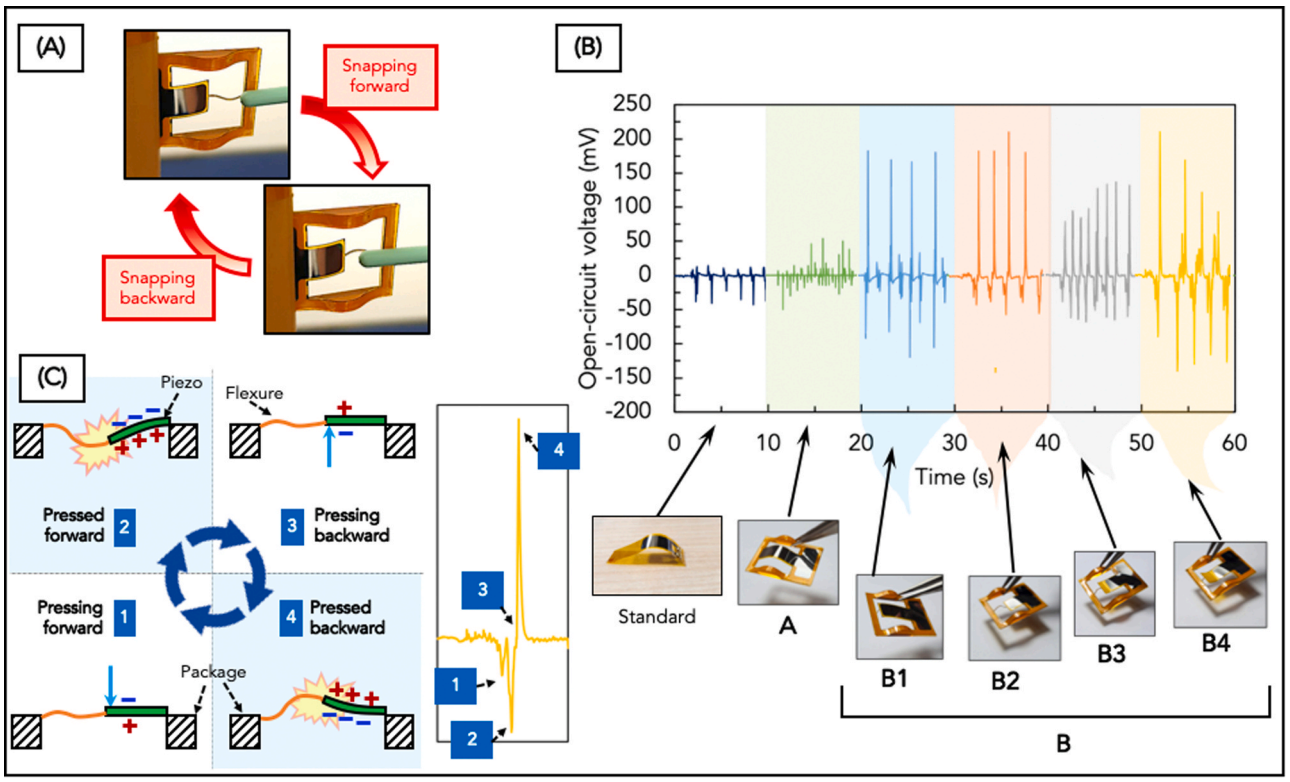

Fig. 9. (A) Snapping forward and backward of a PIP device. (B) Open-circuit voltage of the PIP devices (designs A and B) compared to a standard structure (only subjected to thermal stresses). (C) Working principle of the piezoelectric active element during the snapping cycle with correspondence to the detected signal: (1) pressing forward, (2) pressed forward, (3) pressing backward, (4) pressed backward.

snapping and buckling effect. The device with design A exhibits a lower voltage in comparison to the other PIP designs because of two concurrent factors. First, the higher stiffness of the unstable structure makes it less flexible and less prone to undergo fast snapping, thus reducing the acceleration of the element and consequently the output generation. Secondly, since the piezoelectric region is symmetric with respect to the application point of the mechanical triggering probe (in the middle), the snapping oscillation induces a symmetric stress distribution and thus charges with opposite signs (see also Fig. 2B). This partial charge cancellation effect reduces the amplitude of the output signals.

The presence of the Kapton stripe and the asymmetric design of the PIP devices yield an open-circuit voltage 6÷8 times higher than the one produced by thermal stresses (~45 mV peak-to-peak), demonstrating the enhancement effect of the packaging. In particular, design B4 exhibits an 8-fold-enhanced peak-to-peak voltage of ~350 mV due to the triggered snapping. Noteworthy, the eight-fold enhancement in the output voltage corresponds to a ~64-fold enhancement in the output power with respect to the standard, thermally-stressed device (1.225 μW vs 20.25 nW in a single snapping step, with a 10^5 Ω impedance). This demonstrates that by only modifying some specific features of the design it is possible to enhance power by a factor 64.

The detected signals can be analyzed from a viewpoint of the working mechanism of the fabricated PIP devices, which is illustrated in Fig. 9C for a full snapping cycle. Initially, the device is in an undeformed state, thus there is no potential difference inside the piezoelectric material. Under an applied mechanical stress, caused by a manual tapping or an airflow, the thin film starts to deform generating a piezoelectric potential along the direction of the material polarization, i.e. perpendicularly to the Kapton substrate (Fig. 9C, panel 3). Thus, a positive potential is generated when the applied stress is compressive, increasing from the substrate to the upper surface (where the top electrode is), and reaching the maximum value at the maximum strain (panel 4). When pressing in the opposite direction, the potential follows the same pathway but with opposite sign (panel 1) ending with another snapping step (panel 2). Due to the very fast transition between two equilibrium positions, rapid deformations and high voltages are achieved [70,71]. As a result, the output is much greater than what is achieved in a standard piezoelectric transducer [16].

3.4. Wind energy harvesting performance

In Fig. 11A the results of the wind energy harvesting experiment are reported; the wind speeds used for the tests, and the open-circuit voltage of the tested designs are reported in (i) and (ii-vi), respectively. The output voltage generally increases with increasing wind speed because a higher displacement is imparted to the movement of the piezoelectric active area by a faster airflow. However, it can be seen that even at the greatest wind speeds, device A is not flexible enough to allow for the snapping motion to occur, and thus produces no relevant power output. In contrary, and as a result of the increased flexibility, the variations of design B demonstrate open-circuit voltages in the range of −200÷450 mV.

The open-circuit voltage signals of designs B2, B3 and B4 are reported in Fig. 10A(iv–vi), respectively. At a wind speed of 20 m/s, the devices produce a peak-to-peak voltage of ~0.45 V for B4, ~0.24 V for B2 and ~0.29 V for B3. Therefore, at high speeds the design exhibiting the best performances is B4, allegedly owing to a better interaction between the shortest Kapton flexure and the airflow, which triggers a faster and more impulsive snapping. At lower wind speeds, i.e. 2.5 m/s, the behavior of the three designs is different, in fact the peak-to-peak voltages are ~30 mV for B4, ~25 mV for B2 and ~120 mV for B3. Therefore, B3 with an intermediate length of the Kapton stripe exhibits the best performance for lower speeds.

The design with longer piezoelectric area (design B1) produces a reduced signal, as reported in Fig. 10A(iii), reaching an average peak-to-peak voltage of ~75 mV at 20 m/s, and ~19 mV at 2.5 m/s. The lower

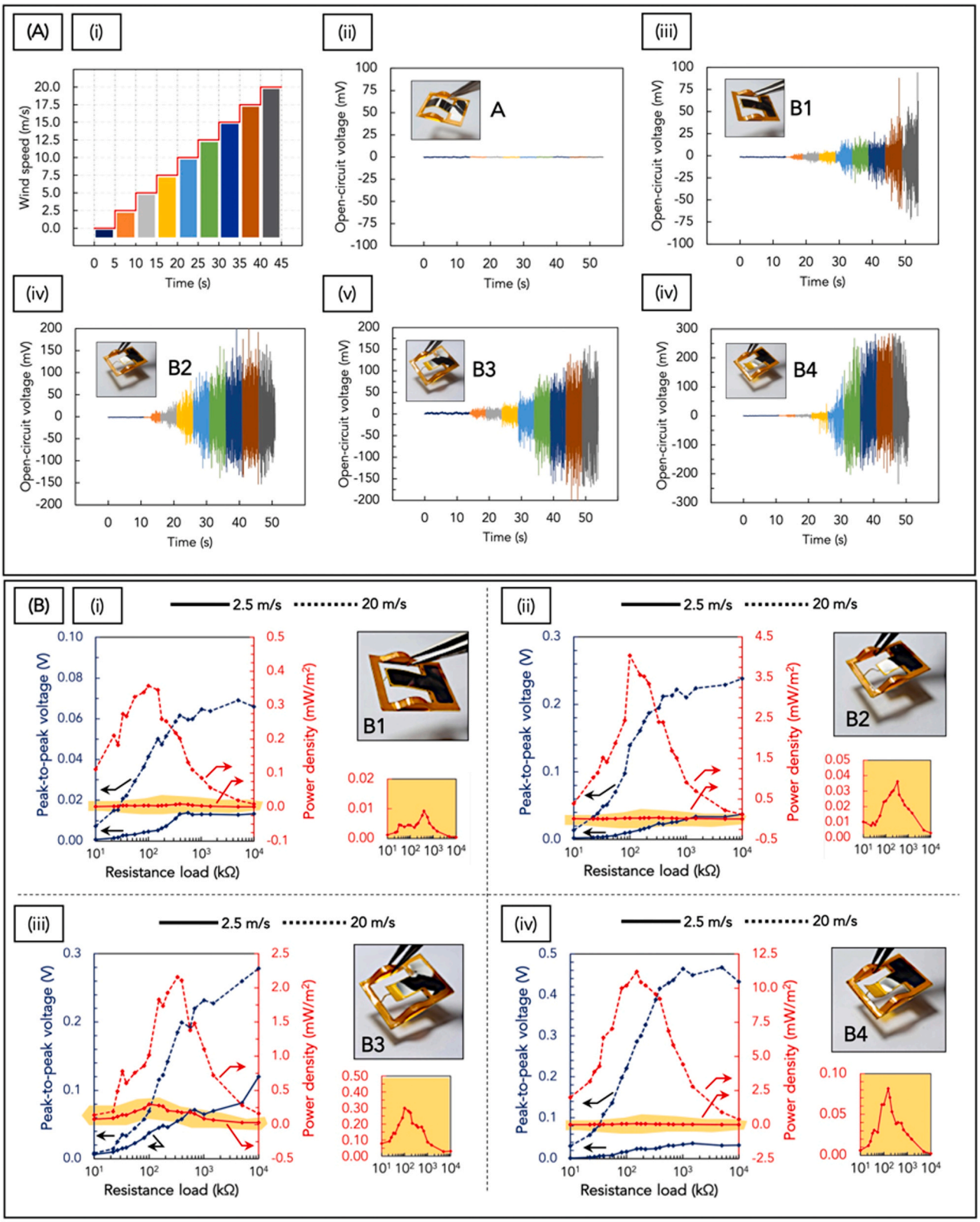

Fig. 10. (A) Open-circuit voltage of the tested designs in the wind tunnel, under a wind speed ramp between 0 and 20 m/s with a step of 2.5 m/s for 5 s (i). Design A (ii), B1 (iii), B2 (iv), B3 (v), B4 (vi). (B) Power density curves and peak-to-peak voltage curves of the tested designs at two selected wind speeds: design B1 (i), B2 (ii), B3 (iii), B4 (iv). The solid lines correspond to a low wind speed (2.5 m/s), whereas the dotted lines correspond to a high wind speed (20 m/s).

voltage is owing to the partial charge cancellation occurring during the oscillation of the long piezoelectric cantilever, which undergoes deformations with opposite curvature during the same movement, i.e. with mechanical stress and thus electrical charges with opposite sign. This demonstrates that a larger area of piezoelectric material is less convenient for a wind energy harvester and, in particular, for the fabrication of a PIP device: the buckling effect resulting from package-induced instability should be imposed not on a full piezoelectric element, but on a substrate on which a smaller piezoelectric element resides.

The previous results are also confirmed by the power density curves given in Fig. 10B(i–iv). After measuring the average peak-to-peak voltage drop on the resistive loads connected to the device, the generated power density can be determined according to the following expression:

$$p = \frac{\langle \Delta V \rangle^2 / \mathscr{R}}{S} \tag{5}$$

where p is the output power density; S is the piezoelectric active area [$S = W(L - L_f)$; see Fig. 2A]; $\mathscr{R}, \langle \Delta V \rangle$ are the resistance and the average peak-to-peak voltage drop on the resistive load, respectively. When the device is connected to an optimal load matching the its electrical impedance [64], the maximum power is reached and the curve exhibits a peak. Fig. 10B reports the power curves for the highest and the lowest wind speeds, i.e. 20 m/s and 2.5 m/s. The curves for design A are not reported because no relevant power was observed. For all the designs the maximum power is achieved at an optimal load of $\sim 10^2$ kΩ. The power density peak at 20 m/s is ~11.3 mW/m^2 for B4, ~4 mW/m^2 for B2, ~2.25 mW/m^2 for B3 and ~0.35 mW/m^2 for B1. At 2.5 m/s, instead, the power peak is achieved at ~0.085 mW/m^2 for B4, ~0.037 mW/m^2 for B2, ~0.30 mW/m^2 for B3 and ~0.01 mW/m^2 for B1. This confirms that (i) design B1 achieves the lowest performances due to partial charge cancellation during motion, (ii) the best design for higher speeds is B4, (iii) the best design for lower speeds is B3. The results are summarized in the Table S2 (Supplementary Information 7).

The energy harvesting efficiency is strictly correlated to the output power, in fact for a piezoelectric transducer invested by a fluid flow it can be determined as the fraction of the wind kinetic energy flux through the cross-section occupied by the harvesting device actually transferred to the output circuit. Therefore, for a single oscillation it can be expressed as follows [72]:

$$\eta = \frac{\widehat{\mathscr{P}}}{\frac{1}{2}\rho v^3 \cdot (2\mathscr{A} W)} \tag{6}$$

where $\widehat{\mathscr{P}}$ is the output power peak of the device; ρ, v are the density and velocity of airflow; W is the width of the active piezoelectric region; $\mathscr{A}$ is the motion amplitude of the active piezoelectric element, thus $2\mathscr{A}$ is the range of motion, which results in 6 mm for design A and ~3 mm for the other designs B1-B4. Hence, the designs B1-B4 can be compared with design A in terms of energy harvesting efficiency η and thus the specific influence of static balancing design onto this parameter can be evaluated. The range of values of the efficiency are below the ones of similar, recently-developed wind energy macro-harvesters, based on other piezoelectric/triboelectric materials or different architectures [73–76]. This is ascribed to the very small device's dimensions under consideration in this work, resulting in relatively low power levels. In addition, Eq. (6) holds for the assumption of a device in a regular flow, not accounting for the whole bluff-body/device system: the calculated efficiency represents a lower limit and specific experimental studies would be required to quantify the contribution of turbulences induced by the bluff body. However, the PIP devices can be rather considered a valid alternative in the context of unstable and nonlinear MEMS energy micro-harvesters, where research efforts are still ongoing [36,77]. In fact, the key aspect on which this work focuses is the relative increase of energy harvesting efficiency induced by the mere application of static balancing principles, as summarized in the Table 3. While the design A has a zero efficiency, the other designs B1-B4 are characterized by an increase in efficiency, which is maximized by design B3 at low speeds (4.6 10^{-3}%) and by design B4 at high speeds (5.24 10^{-4}%). Additionally, it is noteworthy that the efficiency values are generally lower for high speeds while they increase by a factor 10 at low speeds for the same device. This demonstrates the suitability of the proposed method for designing and fabricating innovative future energy harvesters to be adopted especially for weak airflows, where standard technologies or current microfabricated devices cannot work effectively.

A further analysis has been performed to determine the characteristics of the wind-device interaction for lower wind speeds (design B3) and for higher wind speeds (design B4). In particular, a finer ramp of wind speeds has been set for the design B3, within the range of 0÷5 m/s, with a step of 0.1 m/s for a time interval of 1 s. As reported in Fig. 11A, the open-circuit voltage generated by the device B3 increases progressively with increasing wind speeds, exhibiting a low-range cut-in speed of ~0.3 m/s, a low-range threshold speed of ~2.5 m/s and a low-range rated speed of ~4.5 m/s.

The design B4, selected for higher ranges of wind speed, exhibits a threshold speed of 2.5 m/s and a rated speed of ~17.5 m/s (Fig. 11B).

The results demonstrate that slight differences in the design of the PIP device can critically influence its performance. The length of the flexure and the consequent Kapton collector area without the piezoelectric material, are crucial both for imparting the mechanical flexibility of the device and for enhancing the output generation performances in different wind speed ranges. The present work is focused on the preliminary investigation of different designs rather than an optimization of the system for the application of wind energy harvesting. The results shown are useful to provide the following recommendations about the design of buckled devices for mechanical energy harvesting. First of all, the combination of a design aimed at static balancing and the PIP method are a feasible way to increase the flexibility of piezoelectric transducers. Secondly, the presence of the collector in the design can be used to achieve an increased performance: its intermediate flexibility between the flexure and the piezoelectric region provides a more stable oscillation between the stable positions. Finally, it should be noted that the bending-curve of the piezoelectric region is very important for the performance of the device, and may change when the design parameters are manipulated, especially the length of the flexure. When the proposed design is to be optimized for a particular application by tuning for example the flexure length or the length of the collector area, the effect on this curve must also be considered to avoid loss of performance. In general, it is recommended to achieve the desired range of motion and a very low force at switching point in order to design ultra-compliant energy harvesters.

For a first evaluation of the durability of the PIP devices, they have

Table 3
Comparison of output power and energy harvesting efficiency for a single oscillation of the selected designs.

Wind speed (v)		2.5 m/s			20 m/s		
Kinetic power per unit area ($1/2\rho v^3$)		9.57 W/m^2			4.90 kW/m^2		
Design	$2\mathscr{A}W$ (mm^2)	p (mW/m^2)	$\widehat{\mathscr{P}}$ (nW)	η (%)	p (mW/m^2)	$\widehat{\mathscr{P}}$ (μW)	η (%)
A	42	n	n	0	n	n	0
B1	21	0.01	0.21	10^{-4}	0.35	0.02	0.19 10^{-4}
B2	21	0.037	1.13	5.6 10^{-4}	4	0.19	1.88 10^{-4}
B3	21	0.30	9.24	4.6 10^{-3}	2.25	0.11	1.01 10^{-4}
B4	21	0.085	3.92	2.0 10^{-3}	11.3	0.54	5.24 10^{-4}

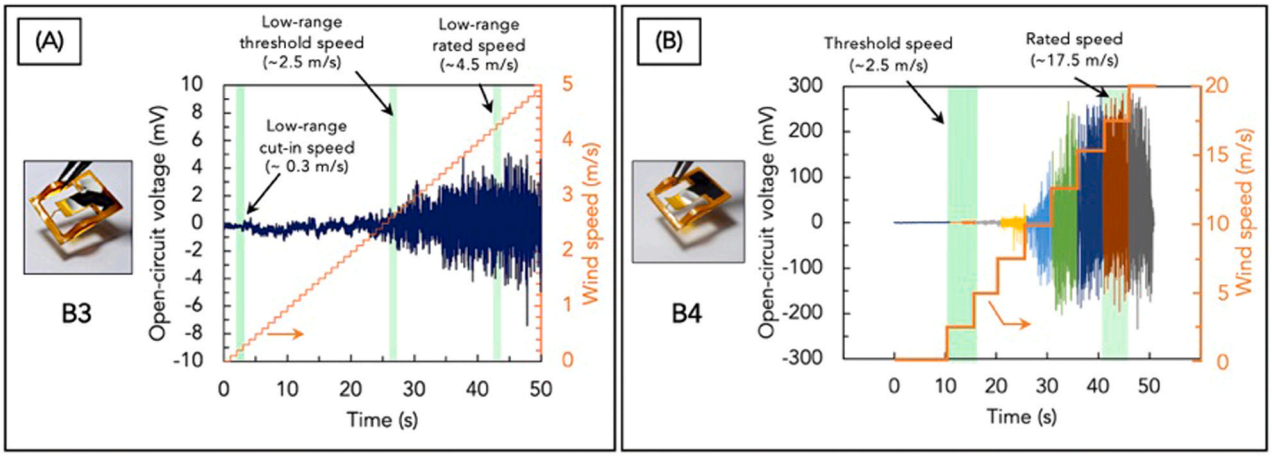

Fig. 11. (A) Fine wind speed ramp for the determination of low-range cut-in, threshold and rated speeds for the design B3. (B) Coarse wind speed ramp for the determination of threshold and rated speeds for the design B4.

been tested in the wind tunnel for a prolonged time interval (10 min) and also after 30 min of continuous flow at a fixed wind speed. In this way, the mechanisms are subjected to the same periodic oscillations and deformations, after a first transient interval. In particular, the mechanisms that exhibited the best results for power densities, i.e. B3 and B4, have been tested at 2.5 m/s and 20 m/s, respectively. As described in Supplementary Information 8 and in Fig. S5(A,B), it can be observed that stable and reproduceable open-circuit voltage signals have been obtained with non-reduced amplitude, which demonstrates the durability of the thin-film materials and also the reliability of the PIP devices.

4. Summary and Conclusions

In this work a new method of inducing out-of-plane buckling in flexible piezoelectric transducers is reported. The method, which is based on the packaging design, is called Package-Induced Preloading (PIP). The theoretical basics of this concept are presented and exploited to develop flexible and lightweight prototypes for low-frequency energy harvesting. The transducers are based on piezoelectric pre-stressed thin films of Aluminium Nitride deposited by MEMS technologies onto a Kapton substrate. The design aimed at static balancing is used to achieve a greatly increased mechanical flexibility. The mechanisms are shaped by laser cutting, and the piezoelectric active area is patterned through lithography. The package extending out-of-plane is fabricated by high-resolution 3D printing.

By mechanically triggering the snapping state on the device, enhanced output voltages are demonstrated in comparison with prior art. A preliminary investigation is reported regarding the influence of the transducers' design onto the output generation performances under incoming wind flows in a wind tunnel. Different designs have been tested and two of them are demonstrated to obtain the best power densities for lower and higher ranges of wind speeds. It was demonstrated that the combination of a design aimed at static balancing and the PIP method is a feasible way to increase the flexibility of piezoelectric transducers. The proposed approach is versatile and can be applied to several types of devices, based also on different materials or structures. It can be harnessed to generate power from unfavourable conditions and to have a greater control on the movements of the piezoelectric structures. The presence of the ~3-mm-thick package as functional mechanical support permits to employ the device in several ways, in confined volumes and spaces or attached onto whichever surface. In addition, the fabricated prototypes were shown to be able to successfully capture energy from an incoming wind flow. Through further optimization, the efficiency of this device can be improved and novel ultra-compliant mechanisms can be designed for applications in energy harvesting from low-frequency mechanical sources, such as wind or water flows and human body motions.

CRediT authorship contribution statement

Massimo Mariello: Conceptualization, Methodology, Validation, Formal analysis, Investigation, Resources, Data Curation, Writing - original draft, Writing - review & editing, Visualization. **Thijs W. A. Blad:** Conceptualization, Methodology, Validation, Formal analysis, Investigation, Resources, Data curation, Writing - review & editing. **Vincenzo M. Mastronardi:** Investigation, Resources. **Francesco Madaro:** Investigation, Resources. **Francesco Guido:** Investigation, Resources. **Urs Staufer:** Validation, Project administration, Supervision, Writing - review & editing. **Nima Tolou:** Validation, Project administration, Supervision, Writing - review & editing. **Massimo De Vittorio:** Validation, Project administration, Supervision, Writing - review & editing.

Declaration of Competing Interest

The authors declare that they have no known competing financial interests or personal relationships that could have appeared to influence the work reported in this paper.

Acknowledgements

The authors would like to acknowledge Dr Donato Cannoletta from the Università del Salento, for his assistance in XRD measurements.

Author Contributions

MM and TB conceived the experiments and wrote the paper; MM fabricated the PIP devices, characterized the AlN material and the 3D printed frames and performed the generation tests; TB performed the mechanical design, FEM simulations and force-deflection measurements; VMM contributed for the fabrication of the 3D printed frames; FM contributed for providing the setup for wind energy harvesting; FG supervised the fabrication of AlN-based transducers; NT, USt and MDV supervised the experiments and the manuscript editing. All authors have read, discussed and edited the manuscript.

Appendix A. Supporting information

Supplementary data associated with this article can be found in the online version at doi:10.1016/j.nanoen.2021.105986.

References

[1] M.T. Todaro, F. Guido, V. Mastronardi, D. Desmaele, G. Epifani, L. Algieri, M. De Vittorio, Piezoelectric MEMS vibrational energy harvesters: advances and outlook, Microelectron. Eng. 183–184 (2017) 23–36, https://doi.org/10.1016/j.mee.2017.10.005.

[2] M.T. Todaro, F. Guido, L. Algieri, V.M. Mastronardi, D. Desmaële, G. Epifani, M. D. Vittorio, Biocompatible, flexible, and compliant energy harvesters based on piezoelectric thin films, IEEE Trans. Nanotechnol. 17 (2018) 220–230, https://doi.org/10.1109/TNANO.2017.2789300.

[3] M. Mariello, F. Guido, V.M. Mastronardi, M.T. Todaro, D. Desmaële, M. De Vittorio, Nanogenerators for harvesting mechanical energy conveyed by liquids, Nano Energy 57 (2019) 141–156, https://doi.org/10.1016/j.nanoen.2018.12.027.

[4] J. Fang, X. Wang, T. Lin, Electrical power generator from randomly oriented electrospun poly(vinylidene fluoride) nanofibre membranes, J. Mater. Chem. 21 (2011) 11088–11091, https://doi.org/10.1039/C1JM11445J.

[5] X. Chen, S. Xu, N. Yao, Y. Shi, 1.6 V nanogenerator for mechanical energy harvesting using PZT nanofibers, Nano Lett. 10 (2010) 2133–2137, https://doi.org/10.1021/nl100812k.

[6] S. Bai, Q. Xu, L. Gu, F. Ma, Y. Qin, Z.L. Wang, Single crystalline lead zirconate titanate (PZT) nano/micro-wire based self-powered UV sensor, Nano Energy 1 (2012) 789–795, https://doi.org/10.1016/j.nanoen.2012.09.001.

[7] P. Wang, H. Du, ZnO thin film piezoelectric MEMS vibration energy harvesters with two piezoelectric elements for higher output performance, Rev. Sci. Instrum. 86 (2015), 075002, https://doi.org/10.1063/1.4923456.

[8] C.-B. Eom, S. Trolier-McKinstry, Thin-film piezoelectric MEMS, MRS Bull. 37 (2012) 1007–1017, https://doi.org/10.1557/mrs.2012.273.

[9] K. Wasa, T. Matsushima, H. Adachi, I. Kanno, H. Kotera, Thin-film piezoelectric materials for a better energy harvesting MEMS, J. Microelectromech. Syst. 21 (2012) 451–457, https://doi.org/10.1109/JMEMS.2011.2181156.

[10] S.S. Won, M. Sheldon, N. Mostovych, J. Kwak, B.-S. Chang, C. Ahn, A. Kingon, I. Won Kim, S.-H. Kim, Piezoelectric poly(vinylidene fluoride trifluoroethylene) thin film-based power generators using paper substrates for wearable device applications, Appl. Phys. Lett. 107 (2015), 202901, https://doi.org/10.1063/1.4935557.

[11] S.-G. Kim, S. Priya, I. Kanno, Piezoelectric MEMS for energy harvesting, MRS Bull. 37 (2012) 1039–1050, https://doi.org/10.1557/mrs.2012.275.

[12] G. Iriarte, J.G. Rodríguez, F. Calle, Synthesis of C-axis oriented AlN thin films on different substrates: a review, Mater. Res. Bull. - Mater. Res. Bull. 45 (2010) 1039–1045, https://doi.org/10.1016/j.materresbull.2010.05.035.

[13] K. Tonisch, V. Cimalla, Ch Foerster, H. Romanus, O. Ambacher, D. Dontsov, Piezoelectric properties of polycrystalline AlN thin films for MEMS application, Sens. Actuators Phys. 132 (2006) 658–663, https://doi.org/10.1016/j.sna.2006.03.001.

[14] E. Iborra, J. Olivares, M. Clement, J. Capilla, V. Felmetsger, M. Mikhov, Piezoelectric and electroacoustic properties of V-doped and Ta-doped AlN thin films, in: Proceedings of the 2013 Joint European Frequency and Time Forum International Frequency Control Symposium (EFTF/IFC); July 2013; pp. 262–265.

[15] K. Tonisch, V. Cimalla, C. Foerster, D. Dontsov, O. Ambacher, Piezoelectric properties of thin AlN layers for MEMS application determined by piezoresponse force microscopy, Phys. Status Solidi C 3 (2006) 2274–2277, https://doi.org/10.1002/pssc.200565123.

[16] F. Guido, A. Qualtieri, L. Algieri, E.D. Lemma, M. De Vittorio, M.T. Todaro, AlN-based flexible piezoelectric skin for energy harvesting from human motion, Microelectron. Eng. 159 (2016) 174–178, https://doi.org/10.1016/j.mee.2016.03.041.

[17] S. Petroni, F. Rizzi, F. Guido, A. Cannavale, T. Donateo, F. Ingrosso, V. M. Mastronardi, R. Cingolani, M. De Vittorio, Flexible AlN flags for efficient wind energy harvesting at ultralow cut-in wind speed, RSC Adv. 5 (2015) 14047–14052, https://doi.org/10.1039/C4RA10319J.

[18] V.M. Mastronardi, F. Guido, M. De Vittorio, S. Petroni, Flexible force sensor based on C-axis oriented aluminum nitride, Procedia Eng. 87 (2014) 164–167, https://doi.org/10.1016/j.proeng.2014.11.609.

[19] S. Petroni, C.L. Tegola, G. Caretto, A. Campa, A. Passaseo, M.D. Vittorio, R. Cingolani, Aluminum nitride piezo-MEMS on polyimide flexible substrates, Microelectron. Eng. 88 (2011) 2372–2375, https://doi.org/10.1016/j.mee.2011.02.080.

[20] S. Petroni, F. Guido, B. Torre, A. Falqui, M.T. Todaro, R. Cingolani, M. De Vittorio, Tactile multisensing on flexible aluminum nitride, Analyst 137 (2012) 5260–5264, https://doi.org/10.1039/c2an36015b.

[21] L. Lamanna, F. Rizzi, F. Guido, L. Algieri, S. Marras, V.M. Mastronardi, A. Qualtieri, M. De Vittorio, Flexible and transparent aluminum-nitride-based surface-acoustic-wave device on polymeric polyethylene naphthalate, Adv. Electron. Mater. 5 (2019), 1900095, https://doi.org/10.1002/aelm.201900095.

[22] A. Iqbal, F. Mohd-Yasin, Reactive sputtering of aluminum nitride (002) thin films for piezoelectric applications: a review, Sensors 18 (2018) 1797, https://doi.org/10.3390/s18061797.

[23] M. Mariello, L. Fachechi, F. Guido, M. De Vittorio, Multifunctional sub-100 μm thickness flexible piezo/triboelectric hybrid water energy harvester based on biocompatible AlN and soft parylene C-PDMS-EcoflexTM, Nano Energy 83 (2021), 105811, https://doi.org/10.1016/j.nanoen.2021.105811.

[24] N. Jackson, L. Keeney, A. Mathewson, Flexible-CMOS and biocompatible piezoelectric AlN material for MEMS applications, Smart Mater. Struct. 22 (2013), 115033, https://doi.org/10.1088/0964-1726/22/11/115033.

[25] P.D. Mitcheson, E.M. Yeatman, G.K. Rao, A.S. Holmes, T.C. Green, Energy harvesting from human and machine motion for wireless electronic devices, Proc. IEEE 96 (2008) 1457–1486, https://doi.org/10.1109/JPROC.2008.927494.

[26] T. Buren, P.D. von Mitcheson, T.C. Green, E.M. Yeatman, A.S. Holmes, G. Troster, Optimization of inertial micropower generators for human walking motion, IEEE Sens. J. 6 (2006) 28–38, https://doi.org/10.1109/JSEN.2005.853595.

[27] P.D. Mitcheson, T.C. Green, E.M. Yeatman, A.S. Holmes, Architectures for vibration-driven micropower generators, J. Microelectromech. Syst. 13 (2004) 429–440, https://doi.org/10.1109/JMEMS.2004.830151.

[28] T.W. Blad, N. Tolou, On the efficiency of energy harvesters: a classification of dynamics in miniaturized generators under low-frequency excitation, J. Intell. Mater. Syst. Struct. 30 (2019) 2436–2446, https://doi.org/10.1177/1045389×19862621.

[29] H. Liu, C. Lee, T. Kobayashi, C.J. Tay, C. Quan, A new S-shaped MEMS PZT cantilever for energy harvesting from low frequency vibrations below 30 Hz, Microsyst. Technol. 18 (2012) 497–506, https://doi.org/10.1007/s00542-012-1424-1.

[30] W. Liu, M. Han, B. Meng, X. Sun, X. Huang, H. Zhang, Low frequency wide bandwidth MEMS energy harvester based on spiral-shaped PVDF cantilever, Sci. China Technol. Sci. 57 (2014) 1068–1072, https://doi.org/10.1007/s11431-014-5511-7.

[31] A.A. Narasimulu, P. Zhao, N. Soin, K. Prashanthi, P. Ding, J. Chen, S. Dong, L. Chen, E. Zhou, C.D. Montemagno, J. Luo, Significant triboelectric enhancement using interfacial piezoelectric ZnO nanosheet layer, Nano Energy 40 (2017) 471–480, https://doi.org/10.1016/j.nanoen.2017.08.053.

[32] H. Liu, F. Zeng, G. Tang, F. Pan, Enhancement of piezoelectric response of diluted Ta doped AlN, Appl. Surf. Sci. 270 (2013) 225–230, https://doi.org/10.1016/j.apsusc.2013.01.005.

[33] M.S. Majdoub, P. Sharma, T. Çağin, Dramatic enhancement in energy harvesting for a narrow range of dimensions in piezoelectric nanostructures, Phys. Rev. B 78 (2008), 121407, https://doi.org/10.1103/PhysRevB.78.121407.

[34] J. Yan, M. Liu, Y. Gyu Jeong, W. Kang, L. Li, Y. Zhao, N. Deng, B. Cheng, G. Yang, Performance enhancements in poly(vinylidene fluoride)-based piezoelectric nanogenerators for efficient energy harvesting, Nano Energy 56 (2019) 662–692, https://doi.org/10.1016/j.nanoen.2018.12.010.

[35] Z.-Z. Ong, V.-K. Wong, J.-H. Ho, Performance enhancement of a piezoelectric rain energy harvester, Sens. Actuators Phys. 252 (2016) 154–164, https://doi.org/10.1016/j.sna.2016.10.035.

[36] Y. Qi, J. Kim, T.D. Nguyen, B. Lisko, P.K. Purohit, M.C. McAlpine, Enhanced piezoelectricity and stretchability in energy harvesting devices fabricated from buckled PZT ribbons, Nano Lett. 11 (2011) 1331–1336, https://doi.org/10.1021/nl104412b.

[37] A.C. Wang, C. Wu, D. Pisignano, Z.L. Wang, L. Persano, Polymer nanogenerators: opportunities and challenges for large-scale applications, J. Appl. Polym. Sci. 135 (2018) 45674, https://doi.org/10.1002/app.45674.

[38] H. Shao, Z. Wen, P. Cheng, N. Sun, Q. Shen, C. Zhou, M. Peng, Y. Yang, X. Xie, X. Sun, Multifunctional power unit by hybridizing contact-separate triboelectric nanogenerator, electromagnetic generator and solar cell for harvesting blue energy, Nano Energy 39 (2017) 608–615, https://doi.org/10.1016/j.nanoen.2017.07.045.

[39] C.R. Bowen, H.A. Kim, P.M. Weaver, S. Dunn, Piezoelectric and ferroelectric materials and structures for energy harvesting applications, Energy Environ. Sci. 7 (2013) 25–44, https://doi.org/10.1039/C3EE42454E.

[40] Z. Yang, S. Zhou, J. Zu, D. Inman, High-performance piezoelectric energy harvesters and their applications, Joule 2 (2018) 642–697, https://doi.org/10.1016/j.joule.2018.03.011.

[41] B. Yang, K.-S. Yun, Piezoelectric shell structures as wearable energy harvesters for effective power generation at low-frequency movement, Sens. Actuators Phys. 188 (2012) 427–433, https://doi.org/10.1016/j.sna.2012.03.026.

[42] L. Dong, C. Wen, Y. Liu, Z. Xu, A.B. Closson, X. Han, G.P. Escobar, M. Oglesby, M. Feldman, Z. Chen, J.X.J. Zhang, Piezoelectric buckled beam array on a pacemaker lead for energy harvesting, Adv. Mater. Technol. 4 (2019), 1800335, https://doi.org/10.1002/admt.201800335.

[43] J. Tao, X. He, S. Yi, Y. Deng, Broadband energy harvesting by using bistable FG-CNTRC plate with integrated piezoelectric layers, Smart Mater. Struct. 28 (2019), 095021, https://doi.org/10.1088/1361-665X/ab2dc2.

[44] N. Tolou, J.A. Gallego, J.L. Herder, Mikroniek (2010) 20–25.

[45] R.P. Middlemiss, A. Samarelli, D.J. Paul, J. Hough, S. Rowan, G.D. Hammond, Measurement of the earth tides with a MEMS gravimeter, Nature 531 (2016) 614–617, https://doi.org/10.1038/nature17397.

[46] N. Tolou, P. Estevez, J.L. Herder, (American Society of Mechanical Engineers Digital Collection)Colline -Type Static. Balance Compliant Micro Mech. (SB-CMM): Exp. Comp. Pre-Curved Straight Beams. June 12, 2012, pp. 113–117.

[47] P.R. Kuppens, J.L. Herder, N. Tolou, Permanent stiffness reduction by thermal oxidation of silicon, J. Microelectromech. Syst. 28 (2019) 900–909, https://doi.org/10.1109/JMEMS.2019.2935379.

[49] L. Algieri, M.T. Todaro, F. Guido, V. Mastronardi, D. Desmaële, A. Qualtieri, C. Giannini, T. Sibillano, M. De Vittorio, Flexible piezoelectric energy-harvesting exploiting biocompatible AlN thin films grown onto spin-coated polyimide layers, ACS Appl. Energy Mater. 1 (2018) 5203–5210, https://doi.org/10.1021/acsaem.8b00820.

[50] M. Mariello, F. Guido, V.M. Mastronardi, R. Giannuzzi, L. Algieri, A. Qualteri, A. Maffezzoli, M. De Vittorio, Reliability of protective coatings for flexible piezoelectric transducers in aqueous environments, Micromachines 10 (2019) 739, https://doi.org/10.3390/mi10110739.

[51] J. Cheng, C. Liu, S. Shang, D. Liu, W. Perrie, G. Dearden, K. Watkins, A review of ultrafast laser materials micromachining, Opt. Laser Technol. 46 (2013) 88–102, https://doi.org/10.1016/j.optlastec.2012.06.037.
[52] B. Luk'yanchuk, N. Bityurin, M. Himmelbauer, N. Arnold, UV-laser ablation of polyimide: from long to ultra-short laser pulses, Nucl. Instrum. Methods Phys. Res. Sect. B Beam Interact. Mater. 122 (1997) 347–355, https://doi.org/10.1016/S0168-583X(96)00759-8.
[53] X. Hu, F. Yang, M. Guo, J. Pei, H. Zhao, Y. Wang, Fabrication of polyimide microfluidic devices by laser ablation based additive manufacturing, Microsyst. Technol. 26 (2020) 1573–1583, https://doi.org/10.1007/s00542-019-04698-4.
[54] Polyimide Films | DuPont Available online: ⟨https://www.dupont.com/electronic-materials/polyimide-films.html⟩.
[55] A. Ruimi, Y. Liang, R.M. McMeeking, Effect of geometry on the performance of MEMS aluminum nitride trampoline resonators in longitudinal resonance, J. Frankl. Inst. 349 (2012) 2294–2312, https://doi.org/10.1016/j.jfranklin.2011.09.005.
[56] M.A. Signore, G. Rescio, C. De Pascali, V. Iacovacci, P. Dario, A. Leone, F. Quaranta, A. Taurino, P. Siciliano, L. Francioso, Fabrication and characterization of AlN-based flexible piezoelectric pressure sensor integrated into an implantable artificial pancreas, Sci. Rep. 9 (2019) 1–11, https://doi.org/10.1038/s41598-019-53713-1.
[57] T.V. Kármán, Aerodynamics, McGraw-Hill, 1963.
[58] A.B. Atrah, M.S. Ab-Rahman, H. Salleh, M.Z. Nuawi, M.J.M. Nor, B.N. Jamaludin, Karman vortex creation using cylinder for flutter energy harvester device, Micromachines 8 (2017) 227, https://doi.org/10.3390/mi8070227.
[59] S. F. Hoerner, Fluid Dynamic Drag: Practical Information on Aerodynamic Drag and Hydrodynamic Resistance, second ed., Hoerner Fluid Dynamics, Bakersfield, 1965. ISBN 978-99911-944-4-8.
[60] C. Zhang, L. Ding, L. Yang, Z. Yang, L. Zhang, Influence of Shape and Piezoelectric-Patch Length on Energy Conversion of Bluff Body-Based Wind Energy Harvester Available online: ⟨https://www.hindawi.com/journals/complexity/2020/3789809/⟩ (Accessed on 14 October 2020).
[61] H.L. Dai, A. Abdelkefi, Y. Yang, L. Wang, Orientation of bluff body for designing efficient energy harvesters from vortex-induced vibrations, Appl. Phys. Lett. 108 (2016), 053902, https://doi.org/10.1063/1.4941546.
[62] A. Roshko, On the wake and drag of bluff bodies, J. Aeronaut. Sci. 22 (1955) 124–132, https://doi.org/10.2514/8.3286.
[63] P. Shen, L. Lin, Y. Wei, H. Dou, C. Tu, Vortex shedding characteristics around a circular cylinder with flexible film, Eur. J. Mech. - B Fluids 77 (2019) 201–210, https://doi.org/10.1016/j.euromechflu.2019.05.008.
[64] S. Priya, Modeling of electric energy harvesting using piezoelectric windmill, Appl. Phys. Lett. 87 (2005), 184101, https://doi.org/10.1063/1.2119410.
[65] F. Chen, M. Jia, Y. She, Y. Wu, Q. Shen, L. Zhang, Mechanical behavior of AlN/Mo functionally graded materials with various compositional structures, J. Alloy. Compd. 816 (2020), 152512,, https://doi.org/10.1016/j.jallcom.2019.152512.
[66] G.F. Iriarte, J. Bjurström, J. Westlinder, F. Engelmark, I.V. Katardjiev, Synthesis of C-axis-oriented AlN thin films on high-conducting layers: Al, Mo, Ti, TiN, and Ni, IEEE Trans. Ultrason. Ferroelectr. Freq. Control 52 (2005) 1170–1174, https://doi.org/10.1109/tuffc.2005.1504003.
[67] S.S. Chauhan, M.M. Joglekar, S.K. Manhas, Influence of process parameters and formation of highly C-axis oriented AlN thin films on Mo by reactive sputtering, J. Electron. Mater. 47 (2018) 7520–7530, https://doi.org/10.1007/s11664-018-6695-6.
[68] A.T. Tran, H. Schellevis, H.T.M. Pham, C. Shen, P.M. Sarro, Influence of seed layer on crystallinity and orientation of pulsed — DC sputtered AlN thin-films for piezoelectric actuators, Procedia Eng. 5 (2010) 886–889, https://doi.org/10.1016/j.proeng.2010.09.251.
[69] P. Cazottes, A. Fernandes, J. Pouget, M. Hafez, Bistable buckled beam: modeling of actuating force and experimental validations, J. Mech. Des. 131 (2009), https://doi.org/10.1115/1.3179003.
[70] G. Tang, B. Yang, C. Hou, G. Li, J. Liu, X. Chen, C. Yang, A piezoelectric micro generator worked at low frequency and high acceleration based on PZT and phosphor bronze bonding, Sci. Rep. 6 (2016) 1–10, https://doi.org/10.1038/srep38798.
[71] W. Wu, H. Du, D.F. Wang, T. Itoh, Resonating characterization of piezoelectric fibers applicable to flexible self-powered fabric, Procedia Eng. 120 (2015) 1028–1031, https://doi.org/10.1016/j.proeng.2015.08.709.
[72] S. Michelin, O. Doaré, Energy harvesting efficiency of piezoelectric flags in axial flows, J. Fluid Mech. 714 (2013) 489–504, https://doi.org/10.1017/jfm.2012.494.
[73] J. Zhang, J. Zhang, C. Shu, Z. Fang, Enhanced piezoelectric wind energy harvesting based on a buckled beam, Appl. Phys. Lett. 110 (2017), 183903, https://doi.org/10.1063/1.4982967.
[74] Y. Feng, L. Zhang, Y. Zheng, D. Wang, F. Zhou, W. Liu, Leaves based triboelectric nanogenerator (TENG) and TENG tree for wind energy harvesting, Nano Energy 55 (2019) 260–268, https://doi.org/10.1016/j.nanoen.2018.10.075.
[75] S. Cui, Y. Zheng, J. Liang, D. Wang, Triboelectrification based on double-layered polyaniline nanofibers for self-powered cathodic protection driven by wind, Nano Res. 11 (2018) 1873–1882, https://doi.org/10.1007/s12274-017-1805-y.
[76] L. Zhao, Y. Yang, Toward small-scale wind energy harvesting: design, enhancement, performance comparison, and applicability, Shock Vib. 2017 (2017) 1–31.
[77] H. Bi, B. Wang, Y. Huang, J. Zhou, Z. Deng, Nonlinear dynamic performance of buckled piezoelectric ribbon-substrate energy harvester, Compos. Struct. 261 (2021), 113570, https://doi.org/10.1016/j.compstruct.2021.113570.